ORIGINAL RESEARCH ARTICLE

Thermal Conductivity of AlSi12/Al_2O_3-Graded Composites Consolidated by Hot Pressing and Spark Plasma Sintering: Experimental Evaluation and Numerical Modeling

ANIL SEQUEIRA, WITOLD WĘGLEWSKI, KAMIL BOCHENEK, THOMAS HUTSCH, AMRITA JAIN, THOMAS WEISSGAERBER, and MICHAŁ BASISTA

Functionally graded metal matrix composites have attracted the attention of various industries as materials with tailorable properties due to spatially varying composition of constituents. This research work was inspired by an application, such as automotive brake disks, which requires advanced materials with improved wear resistance on the outer surface as combined with effective heat flux dissipation of the graded system. To this end, graded AlSi12/Al_2O_3 composites (FGMs) with a stepwise gradient in the volume fraction of alumina reinforcement were produced by hot pressing and spark plasma sintering techniques. The thermal conductivities of the individual composite layers and the FGMs were evaluated experimentally and simulated numerically using 3D finite element (FE) models based on micro-computed X-ray tomography (micro-XCT) images of actual AlSi12/Al_2O_3 microstructures. The numerical models incorporated the effects of porosity of the fabricated AlSi12/Al_2O_3 composites, thermal resistance, and imperfect interfaces between the AlSi12 matrix and the alumina particles. The obtained experimental data and the results of the numerical models are in good agreement, the relative error being in the range of 4 to 6 pct for different compositions and FGM structure. The predictive capability of the proposed micro-XCT-based FE model suggests that this model can be applied to similar types of composites and different composition gradients.

https://doi.org/10.1007/s11661-024-07506-5

I. INTRODUCTION

THE metal–ceramic-graded composite materials are designed to improve thermal properties, corrosion resistance, and mechanical strength depending on the target application.[1] They can resist high-temperature gradients and are proficient in reducing thermal stresses. Smooth transition in thermomechanical properties prevents issues related to delamination and cracking.[2] The aluminum-alumina-graded composites, such as AlSi12/Al_2O_3 studied in this paper, are of particular interest for structural applications due to their light weight, excellent wear resistance, high strength, and thermal stability. The thermal properties of aluminum–alumina-graded composites are critical to their performance in high-temperature environments, such as brake systems, where heat must be removed as quickly as possible. The AlSi12 matrix exhibits enhanced mechanical and heat transport properties, while the Al_2O_3 reinforcement provides excellent wear resistance. Therefore, the spatially varying composition of AlSi12/Al_2O_3 is designed to take advantage of the properties of each of its constituents, resulting in material properties essential for modern automotive brake disk application.

Heat transfer and temperature changes are prevalent in most physical and chemical processes. Therefore, it is reasonable to study thermal conductivity, a fundamental property in the behavior of materials involved in heat transfer caused by frictional wear. For metal–ceramic stepwise-graded materials, the overall thermal conductivity depends on thermal conductivity of its constituents, their volume fractions, and gradient distribution of each layer. It is possible to control the overall thermal conductivity of a graded composite by

ANIL SEQUEIRA, WITOLD WĘGLEWSKI, KAMIL BOCHENEK, AMRITA JAIN, and MICHAŁ BASISTA are with the Institute of Fundamental Technological Research, Polish Academy of Sciences, Pawińskiego 5 B, 02-106 Warsaw, Poland. Contact e-mail: mbasista@ippt.pan.pl THOMAS HUTSCH is with the Fraunhofer Institute for Manufacturing Technology and Advanced Materials, Winterbergstrasse 28, 01277 Dresden, Germany. THOMAS WEISSGAERBER is with the Fraunhofer Institute for Manufacturing Technology and Advanced Materials and also with the Institute of Material Science, TUD Dresden University of Technology, Helmholtzstrasse 7, 01062 Dresden, Germany.
Manuscript submitted November 17, 2023; accepted June 25, 2024.

Published online: 18 July 2024

designing the composition, number, and sequence of layers. Therefore, the focus of the research reported in this paper was to investigate the thermal conductivity AlSi12/Al_2O_3-graded composites and to provide explanations for the physical effects observed in fabrication and experiments.

The proper choice of the processing route is crucial as it significantly affects the microstructure and thus the thermal properties. Recently, several experimental studies have been conducted to investigate the thermal properties of graded metal–ceramic composites using different processing methods to achieve a continuous or stepwise gradient. An overview of the manufacturing methods, applications, and future challenges for the graded materials has been reported in References 3, 4.

Hot pressing (HP) and spark plasma sintering (SPS) are two powder metallurgy techniques that are widely used to produce metal matrix-graded composites.[5,6] HP uses pressure and a conventional heating source to densify composite powders, while SPS uses pulsed electric current to rapidly heat the powders under applied pressure, resulting in rapid densification and typically minimal grain growth in a short sintering time. It has been shown in Reference 7 that the thermal conductivity of α-Al_2O_3-reinforced aluminum matrix particulate composites produced by conventional powder metallurgy processes can be improved by varying the volume fraction and particle size of Al_2O_3. A comparative study of the thermal conductivity of AlSi12/Al_2O_3 composites obtained by squeeze casting of molten AlSi12 alloy into porous ceramic preforms and by hot pressing is presented in Reference 8. This study showed that the composites produced by squeeze casting have superior thermal conductivity, lower thermal residual stresses, and lower frictional wear than those produced by hot pressing. Another study of an AlSi12/Al_2O_3-infiltrated ungraded composite showed that the thermal conductivity decreased with increasing temperature for different amounts of the pore-forming agent.[9] The studies on four-layer Al/Al_2O_3 FGM samples obtained by cold compacting followed by hot pressing[10] and five-layer Al/Al_2O_3 FGM samples obtained by spark plasma sintering[11] were focused on the mechanical properties of these multilayer materials. In recent years, the SPS technique has been extensively used to develop Al matrix FGMs reinforced with alumina[12,13] or silicon carbide.[14] Other fabrication techniques such as centrifugal casting and tape casting have also been used to produce Al matrix FGMs.[15–17] However, little attention has been paid to the effect of the metal–ceramic interfaces and the thermal response of these multilayer composites. In our research, the layered AlSi12/Al_2O_3 composites with different alumina contents were fabricated by HP and SPS techniques to perform a comparative analysis of their thermal conductivities.

Pores in composite materials can significantly affect their thermal conductivity. The size, shape, and distribution of the pores are essential factors that must be taken into account. Larger pores and higher concentrations of pores will result in a lower thermal conductivity. By introducing the ceramic reinforcement (*e.g.*, Al_2O_3) into the metal matrix, the densification of the composite is reduced.[18] It was reported that the relative density of fully dense composites decreased to 95 pct as the Al_2O_3 content in the Al matrix was increased.[19] High compacting pressures resulted in high relative densities and lower porosity, while porosity increased with higher Al_2O_3 content.[20] Obviously, the porosity of aluminum matrix composites obtained by HP and SPS techniques depend on the process parameters such as sintering temperature, pressure, heating rate, holding time, and particle size and distribution. Therefore, the current study also analyzes the effect of porosity on the thermal conductivity of AlSi12/Al_2O_3 FGMs produced by HP and SPS.

Over the past few decades, a variety of modeling approaches have been used for the investigation of the thermal properties of FGMs. The most popular empirical, analytical, and numerical models for predicting the effective thermal conductivity of composite materials using the properties and volume fractions of constituent phases are reviewed in Reference 21. Numerical models for the thermal properties of graded composites are often used because the intricate shapes of inclusions, especially in composites fabricated by powder metallurgy techniques do not lend themselves easily to analytical modeling. The finite element method (FEM) was used to solve thermal problems for various types of inclusions. However, obtaining accurate numerical solutions for composites through complex domain discretization requires a lot of finite elements. In [22–24] homogenization based on the finite element method used a 3D FE unit cell to accurately calculate the effective thermal conductivity of FGMs. In these studies, the unit cell represented the smallest repeating structure of the crystalline material describing periodic arrangements to determine the effective properties of the material. A good correlation between the FEM results and the experimental measurements was obtained. Two-dimensional FE microstructures were implemented in ABAQUS™ to numerically determine the effective properties of Al/Al_2O_3 composites.[24] This study showed detailed 2D microstructural morphologies of the composites used in the FE modeling that efficiently captured the thermal effects.

Interfacial thermal resistance is one of the barriers to achieve higher thermal conductivity in metal matrix composites. Thermal transport across a metal–ceramic interface is governed by the interplay between the different heat carriers. In the metal matrix, heat is transferred by both electrons and phonons, whereas in the ceramic phase, phonons are the dominant heat transfer mechanism. The reflection and scattering of the heat carriers occurring at the metal/ceramic interface can have a significant effect on the thermal conductivity of a composite.[25] Interfacial thermal conductance h_K (or its reciprocal, interfacial thermal resistance R_K), defined as a ratio of the heat flux over the temperature drop across the interface, is a critical property in heat transport processes in heterogeneous materials such as MMCs. Comprehensive reviews of the experimental methods and computational models used to evaluate the h_K at atomistic, nanometric, and micron scale can be found in References 26, 27. A discrete element model

was established in Reference 28 for thermal conductivity of a graded composite made of porous alumina preform infiltrated by a molten Al alloy. The authors investigated the effect of the thermal contact resistance and found out that the thermal conductivity of the composite was extremely sensitive to the presence of imperfect interfaces which could be reduced by increasing the interconnection size between particles.

The effect of porosity on the thermal conductivity can be used to optimize the microstructure of the material for specific thermal conductivity requirements or to design new materials with tailored thermal properties. A numerical model based on FEM in a 3D space has been used to evaluate the influence of the porosity on the thermal conductivity of the composite, with good agreement with experimental data.[29]

From this brief review of the literature, it is clear that a considerable amount of research, both experimental and modeling, has been conducted on the thermal conductivity of Al/Al_2O_3-graded composites. However, assumptions have been made about ceramic particle size, shape and uniformity of dispersion in the metal matrix, and limited research has been done on interfacial thermal conductance in the case of numerical modeling.

The aim of the present study is twofold: (i) experimental evaluation and comparative analysis of the thermal conductivity of $AlSi12/Al_2O_3$-graded composites (FGMs) prepared by two powder metallurgy techniques (HP and SPS), and (ii) numerical simulations of the thermal conductivity of FGMs by the finite element method (FEM) using the actual material microstructure images reconstructed from micro-computed tomography (micro-XCT). The effects of graded microstructure, porosity, and interfacial thermal conductance on the thermal conductivity of the $AlSi12/Al_2O_3$ composite layers and FGMs are analyzed. The micro-XCT-based FEM models of the thermal conductivity are validated by comparison with the experimental measurements.

II. MATERIALS AND METHODS

A. *Processing of AlSi12 Matrix FGMs Reinforced with Al_2O_3 Particles*

The study material was a stepwise-graded aluminum matrix composite $AlSi12/Al_2O_3$ (FGM) consisting of three AlSi12 layers containing 10, 20, and 30 vol pct of alumina particles. This composition of the FGM was chosen to study the effect of the layered graded structure on the thermal conductivity for this particular $AlSi12/Al_2O_3$ composite system. It is a kind of "model" composition to reveal essential features of the thermal conductivity of the graded $AlSi12/Al_2O_3$ material. For a real application in brake disks, it would be necessary to determine an optimal structure of the FGM that would, on the one hand, effectively dissipate the heat generated during braking and, on the other hand, ensure reduced residual stresses in the bulk while improving the wear resistance of the outer surface of the disk. The individual composite layers and the FGM were prepared by the powder metallurgy method using commercial powders of AlSi12 (NewMetKoch, average particle size 5 μm, purity 99.99 pct) and Al_2O_3 (Goodfellow, average particle size 10 μm, purity 99.99 pct). AlSi12 was selected as the matrix material due to its advantageous mechanical and thermal properties that make it attractive to the automotive industry. The raw AlSi12 powder consisted mainly of two elements, 12.1 wt pct Si and 87.9 wt pct Al, which is equivalent to the commercially available AlSi12 alloy. The EDS spectrum and SEM image of the AlSi12 powder are presented in Figure 1. A schematic diagram and the associated labels (A through G) of the single-layer, two-layer, and three-layer samples are shown in Figure 2.

The powder mixtures were prepared using a planetary ball mill (Pulverisette 5 Fritsch) with 250 mL vials and Ø10 mm tungsten carbide milling balls. In order to obtain a homogeneous distribution of the ceramic particles in the aluminum matrix, the mixing process was carried out under the following conditions: rotational speed $\omega = 100$ rpm, ball-to-powder weight ratio (BPR) 5:1, mixing time 5 hours. Prior to the milling process, the powders were sealed under an inert atmosphere inside the environmental chamber to avoid oxygen contamination during the milling process, and the vials were filled to ½ full with heptane. After milling, the powders were dried in a vacuum oven to remove the liquid medium. Prior to sintering, each layer of the FGM was individually cold-pressed under a pressure of 100 MPa and carefully stacked to form a single sample of multilayer composites. This step further smoothed the interphase between the layers after the sintering process.

The powder mixtures were then compacted using hot pressing (HP) and spark plasma sintering (SPS) techniques. In both techniques, uniaxial pressure is applied to powder mixtures stacked in a graphite die, but the heat source in each technique is different. HP sintering uses an external graphite heating element, while SPS uses a high-pulsed electric current to heat the graphite die, stamps, and powder, inducing Joule heating.[30] SPS is applicable to electrically conductive powders such as $AlSi12 + xAl_2O_3$ ($x = 10$, 20, 30 vol pct) studied in this paper, as well as non-conductive powders.[31] In the latter case, heat is transferred from the tool to the sample by thermal conduction.

The optimum values of the HP and SPS process parameters were determined experimentally to obtain the composite samples with a minimum relative density of 96 pct. For hot pressing, the process was performed in a Thermal Technology LLC hot press in a vacuum atmosphere using a graphite mold at a temperature of 560 °C, with a heating rate of 5 °C/min, a sintering pressure of 30 MPa, and a dwell time of 180 minutes. The process parameters for spark plasma sintering were as follows: sintering temperature 502 °C, pressure 40 MPa, heating rate 70 °C/min, and dwelling time 10 minutes. In both sintering processes, HP and SPS, free cooling to room temperature was applied. The process parameters were carefully selected and controlled in order to achieve the best compaction possible without damaging the equipment. To avoid overheating of the AlSi12 material during the fast SPS process, which could lead to AlSi12 melting, the dwelling temperature was

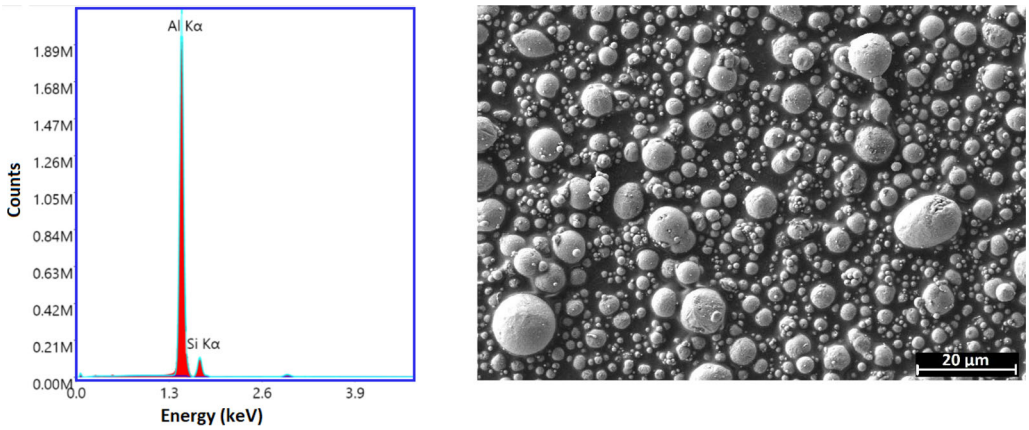

Fig. 1—(*a*) EDS spectrum of the Al–Si powder mixture, (*b*) SEM image of the as-received AlSi12 powder.

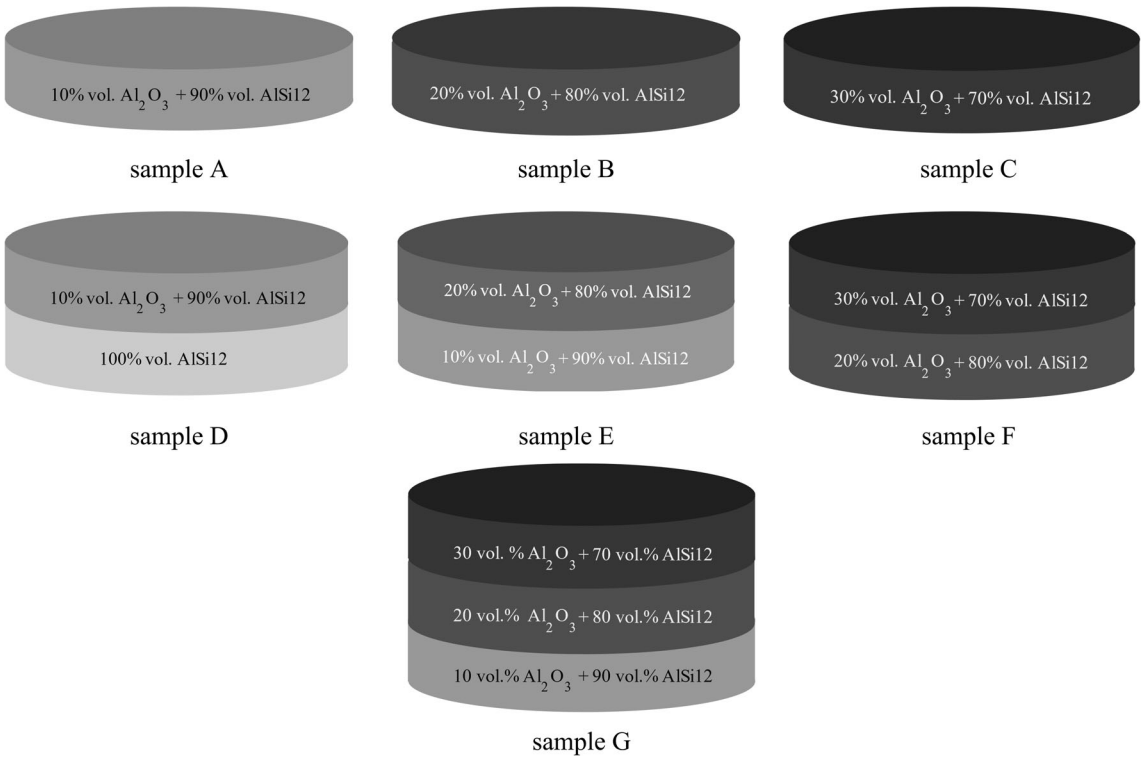

Fig. 2—Scheme of layered AlSi12/Al_2O_3 composite materials with 10, 20, and 30 pct volume content of Al_2O_3. Each layer was approximately 1 mm thick.

lowered while the sintering pressure was increased compared to the HP process parameters. This point is further discussed in Section IV–B. The sample thicknesses of the single-layer, two-layer, and three-layer materials were 1, 2, and 3 mm, respectively.

B. *Microstructure Characterization*

In order to analyze the microstructure of the AlSi12/Al_2O_3 composites in detail, the samples were cut using a wire cutter at one-quarter of the diameter and along the thickness of the layer. Next, the samples were ground and polished along the cross-sectional direction. The microstructure was then analyzed by scanning electron microscopy using the ZEISS Crossbeam 350 system.

In addition, X-ray micro-computed tomography (micro-XCT) was performed on the Nanotom M (Phoenix/GE) system, which has been shown to provide high quality images for similar metal–ceramic composites.[32] This non-destructive imaging technique is capable of accurately reproducing the 3D microstructure of materials, which is then used as input data for FE meshes in numerical simulations. The micro-XCT scanning was performed using a GE Phoenix Nanotom M device at

the Materials Center Leoben (Austria). The applied voltage was 160 kV, the current was 135 mA, the voxel size was 1 micron, the sample dimensions were $1 \times 1 \times 1$ mm^3, and the source-to-target distance was 2.3 mm.

C. *Density Measurements*

The relative densities of the HP and SPS composite samples were evaluated using the Archimedes' method. The theoretical density of the composites was defined using the density of AlSi12 = 2.656 g/cm^3 calculated assuming the densities for Al and Si equal 2.7 and 2.33 g/cm^3, respectively. The density of Al_2O_3 = 3.95 g/cm^3 was obtained from experimental measurements on pure alumina powder sintered in hot press at 1450 °C/1 h/30 MPa, which resulted in a pore-free microstructure. The immersion liquid was distilled water at a temperature of 22 °C, with a density of 0.9978 g/cm^3.

The porosities of the AlSi12/Al_2O_3 composite layers were calculated from their relative densities.[33,34] In addition, the starting powders of AlSi12 and Al_2O_3 were analyzed for the presence of nanometric pores by the gas adsorption method. The adsorption–desorption isotherms were recorded on the AutoSorbiQ, Quantachrome analyzer with N_2 adsorption at − 196 °C and ASQWIN software.

D. *Experimental Evaluation of Thermal Conductivity*

Thermal conductivity was determined from the measured thermal diffusivity of the fabricated composite layers and the FGMs. Thermal diffusivity was measured by the laser flash technique using a Netzsch LFA 457 device in the temperature range of 25 °C to 300 °C in an argon atmosphere.

The equation used for the calculation of thermal conductivity is expressed as follows:

$$\lambda = \rho\, c_p D, \qquad [1]$$

where λ is the thermal conductivity in W/mK, ρ is the density in g/cm^3, c_p is the specific heat in J/gK, and D is the diffusivity in mm^2/s.

E. *Analytical Estimation of Thermal Conductivity of FGMs*

An analytical estimate of the thermal conductivity of stacked composite layers can be obtained by using the Reuss approximation,[35] without considering interactions between adjacent layers. The analytical maximum effective thermal conductivity was calculated from the experimentally measured thermal conductivity of each material acting as the layer material.

The effective thermal conductivity of n layers connected in series and oriented perpendicular to the direction of the thermal conductivity measurement is given by the following formula[29]:

$$\lambda_{\text{eff}} = \frac{t_{\text{eff}}}{\left[\frac{t_1}{\lambda_1} + \frac{t_2}{\lambda_2} + \frac{t_3}{\lambda_3} + \dot{s} + \frac{t_n}{\lambda_n}\right]}, \qquad [2]$$

where λ_{eff} is the effective thermal conductivity of the graded composite, t_{eff} is the total thickness of the composite, $t_1, \ldots, t_n$ and $\lambda_1, \ldots \lambda_n$ are the thicknesses and conductivities of the individual layers, respectively.

III. NUMERICAL MODELING DETAILS

The thermal conductivity of the AlSi12/Al_2O_3-graded composites was modeled using the finite element method (FEM) which requires meshing to perform numerical simulations. First, micro-XCT was used to reconstruct the actual material microstructure without making any assumptions about the size, shape, and spatial distribution of the reinforcing ceramic particles, since all of this information is captured by micro-XCT. The FE mesh was then generated using the micro-XCT data and a commercial image processing tool. Finally, the FE model was implemented in Abaqus[36] to compute the thermal flux from which the thermal conductivity is calculated. These steps are detailed below.

A. *Mesh Generation*

The obtained micro-XCT digital data were applied to generate the FE meshes mimicking the actual microstructure of the samples using a commercial image processing tool Simpleware™ software (Version 4.7; Synopsys, Inc., Mountain View).[37] One voxel from a micro-XCT image was represented by one cubic finite element of $1 \times 1 \times 1$ μm^3. More details on this approach can be found in References 29, 32, 38. Based on the micro-XCT images, cubic and tetrahedron meshes were developed (Figure 3), which made it possible to numerically analyze the effect of the element type on the effective thermal conductivity of the graded composites.

In the AlSi12/Al_2O_3 composites studied, the small difference in density of the phase materials made it difficult to obtain a clear boundary between AlSi12 and Al_2O_3 grains using micro-XCT. It is known that in micro-XCT there is an interplay between the voxel size and the contrast. For our modeling purposes, the voxel size of 1 micron provided satisfactory contrast and a good representation of the microstructure of AlSi12/Al_2O_3. We also performed the micro-XCT experiments with a voxel size smaller than 1 micron. This resulted in finer microstructure images but at the expense of the contrast between the phase materials. As a result, it was not possible to generate a finite element mesh using the SCAN IP/FE software from the micro-XCT data obtained with the voxel size smaller than 1 micron. Based on our previous experience,[32] a threshold-based grayscale segmentation of the SCAN IP/FE software was used to build the model, which required an appropriate level of contrast in the scans. Validation of the segmentation consisted of comparing the volume

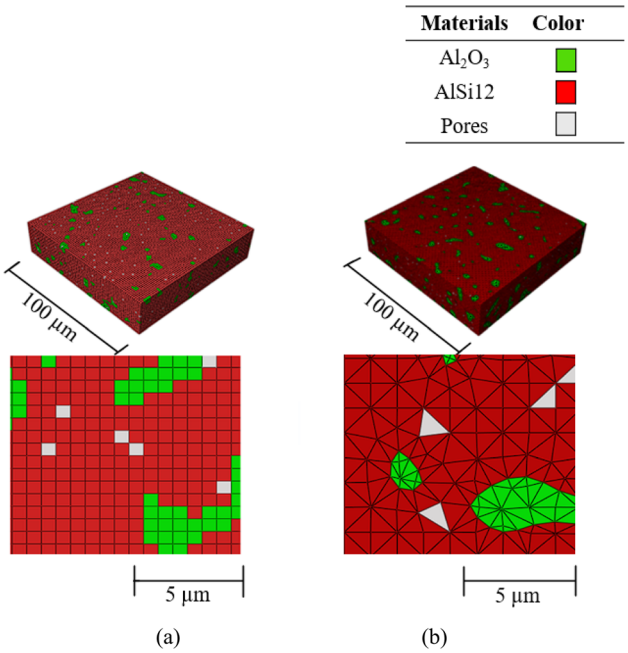

Fig. 3—Types of mesh based on the micro-XCT images (*a*) cubic elements (*b*) tetrahedron elements.

occupied by Al_2O_3 in the sintered composite with the volume occupied by the elements representing the Al_2O_3 phase in the RVE. The difference between the volumes in the sintered composite and the RVE was less than 0.5 pct for all Al_2O_3 contents.

In order to study the effect of porosity on the effective thermal conductivity of the composite layers and the FGMs, the porosities obtained from the experimental measurements for AlSi12 + 10vol pct Al_2O_3, AlSi12 + 20vol pct Al_2O_3, and AlSi12 + 30vol pct Al_2O_3 were implemented in the finite element models. The pores were assumed to be uniformly distributed in the AlSi12 matrix and filled with air, with an estimated thermal conductivity of air equal to 0.025 W/mK.[39] The porosity of the material generally leads to a reduction in thermal conductivity. However, for the samples consolidated by hot pressing (Figure 4), the effect of porosity on the effective thermal conductivity was less pronounced due to the very high relative densities of these samples.

Figure 5 shows the influence of the type of finite elements, cubic *vs* tetrahedron, of ungraded AlSi12/Al_2O_3 composites sintered by the HP [Figure 5(a)] and SPS [Figure 5(b)] on the effective thermal conductivity. It is evident that the tetrahedron elements used in the micro-XCT-based FE model give better numerical results for λ_{eff} for both HP and SPS composites. Therefore, the cubic model was not used in the further simulations of the effective thermal conductivity.

B. *Estimation of the Interfacial Thermal Conductance*

When heat is transferred through a material, it primarily occurs through lattice vibrations or phonons. In composites, grain boundaries scatter phonons mainly due to the interfacial thermal barriers between metal and ceramic, causing them to lose energy and reduce the overall thermal conductivity of the material.[40] From the SEM images, it was observed that the interfaces between the metal matrix and ceramic particles were rougher for SPS samples than for HP samples, and the number of interfaces was large. The bonding between the matrix and the reinforcement, which is correlated with the HP and SPS processes, could also affect the thermal conductivities. These facts should be considered when modeling the thermal conductivity of the graded composites. Therefore, an imperfect interface FE model was developed taking into account the effect of interfacial thermal resistance. Such models have been found in the prediction of the thermal conductivity of metal–ceramic composite materials with imperfect interfaces.[41,42] Estimating the interfacial thermal conductance at the microscale for layered composites is experimentally difficult and requires sophisticated equipment.[43] Alternatively, the interfacial thermal conductance can be estimated using the classical mean field scheme of Maxwell[44] and the differential effective medium (DEM) scheme of Bruggeman.[45] In our study, the interfacial thermal conductance value of 0.01 MW/m^2K was taken from a rigorous experimental test of atomistic-level theories for the interfacial thermal conductance between aluminum and alumina.[46] Reference 46 provides the interfacial thermal conductance of the aluminum–alumina interface using interfacial conductance modal analysis and atomistic green function method and compares it with the experimental time-domain thermoreflectance data, experimental data obtained by Stoner and Maris,[47] another set of experimental data reported by Hopkins *et al.*[48] as well as the diffuse mismatch model predictions.[49] In particular, the interfacial conductance modal analysis predictions showed very good agreement with the experimental data for aluminum–alumina composite, hence they were adopted in our study for the modeling purposes. The assumption of nearly perfect adherence at the Al_2O_3–AlSi12 interfaces is supported by the SEM images in Figure 6.

Figure 7 shows the implementation of the interaction properties defined in Abaqus at the interfaces between metal and ceramic in a single composite layer (sample A, see Figure 2). The yellow symbols in Figure 7 are the graphical representation of the contacts between two deformable bodies in ABAQUS when some contact properties are applied. This can be done using the module named "Interactions" in ABAQUS/Standard simulations. A perfect interface is an idealized interface between the metal and ceramic phases, where there is no interfacial thermal resistance or barrier to heat transfer. The increase in the volume fraction of the ceramic particles is reflected in an increase in the area of the interfaces per unit volume of the composite. This reduces the interfacial thermal conductance and, as a result, the thermal conductivity.[50] Similar behavior was also observed in Reference 51 due to a higher Si content in Al–Si composites. Figure 8 shows the effect of the interfacial thermal conductance on the effective thermal conductivity as predicted by the micro-XCT FEM

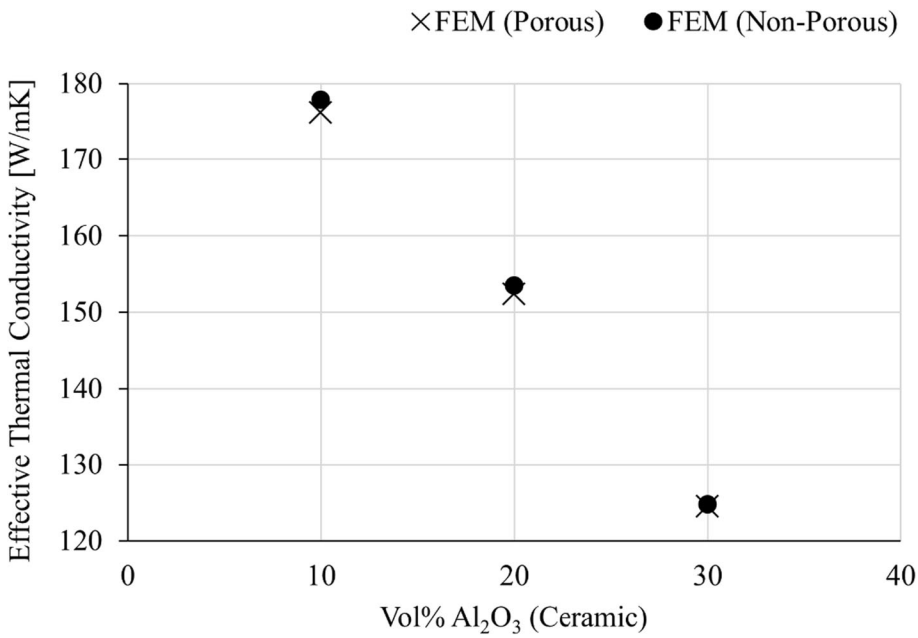

Fig. 4—Effect of porosity on the effective thermal conductivity of the HP samples according to the micro-XCT-based FE model implemented in Abaqus[36].

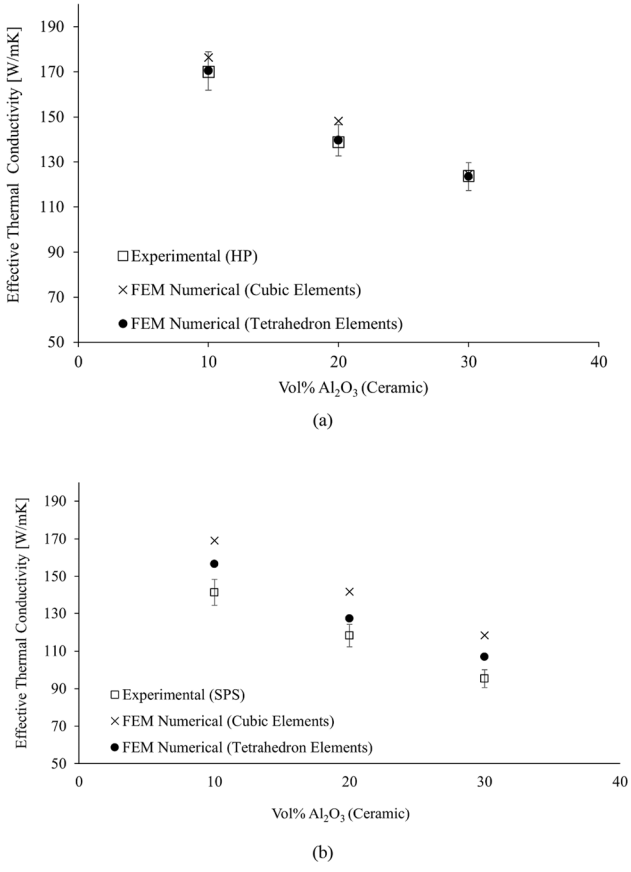

Fig. 5—Comparison of the predictive capability of the cubic element *vs* the tetrahedron element micro-XCT-based FEM models used to calculate the effective thermal conductivity of ungraded AlSi12/Al_2O_3 composite layers with different alumina volume fraction fabricated by (*a*) HP and (*b*) SPS.

model for 10, 20 pct, and 30 vol pct of Al_2O_3 in the AlSi12/Al_2O_3 composites.

C. *Micro-XCT FEM Modeling of Thermal Conductivity of Graded Composites*

The FE model was developed using Abaqus™ software.[36] The finite element meshes were generated from micro-XCT scans of the microstructure of the samples. Figure 9 shows the mesh models for the three-layer FGM and Figure 10 shows the single-layer composite fabricated by the HP.

Hexagonal, eight-node thermal elements were used to solve the linear Fourier heat conduction equation in a three-dimensional domain:

$$q = -\lambda_{\text{eff}} T, \qquad [3]$$

where q is thermal flux, λ_{eff} is effective thermal conductivity, and $T = T_{\text{hot}} - T_{\text{cold}}$. The temperature on the two opposite faces of the specimen was kept constant, wherein one of the faces was assumed to be hot ($T_{\text{hot}} = 100$), and the other face to be cold ($T_{\text{cold}} = 0$). The remaining specimen's faces were characterized by the adiabatic state.

In Figure 9 some of the Al_2O_3 domains appear continuous across the layer interfaces. When finite elements containing Al_2O_3 come into contact with other Al_2O_3 elements at the interfaces during the layer stacking process in Functionally Graded Material (FGM) modeling using ABAQUS, a continuous Al_2O_3 domain is formed across these interfaces. This continuity arises from the merging operation involved in ABAQUS, where different layers are stacked together, resulting in a seamless Al_2O_3 domain that spans across the interface boundaries.

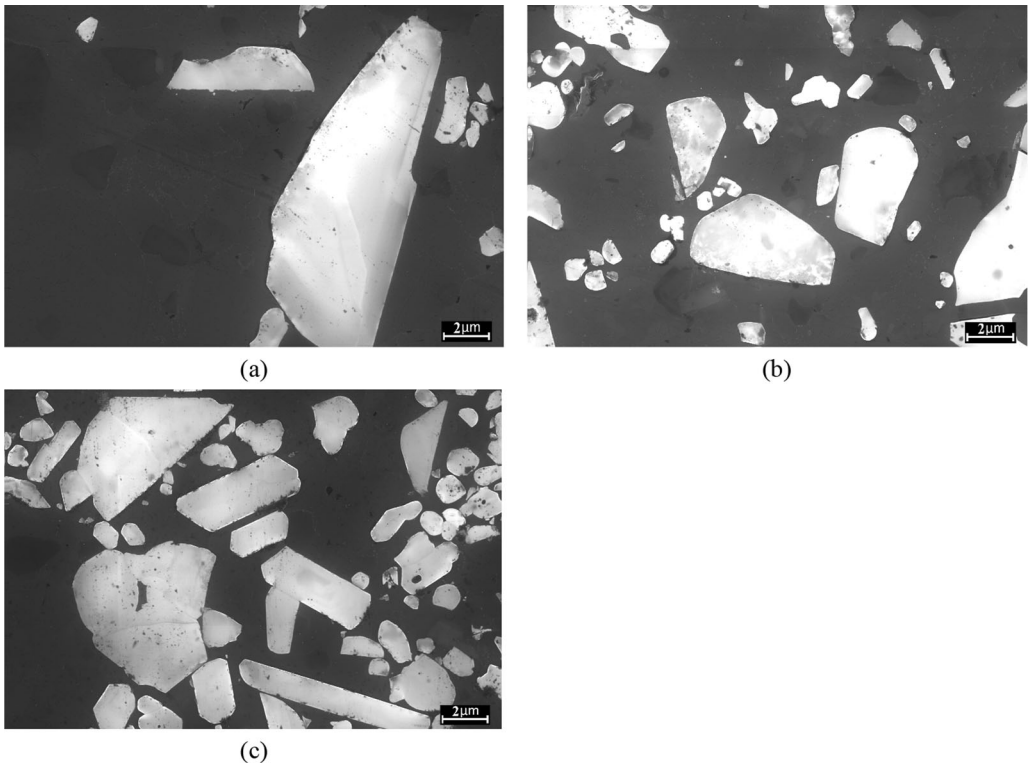

Fig. 6—SEM images showing the adhesion of the AlSi12 matrix to the Al_2O_3 reinforcement in (*a*) AlSi12 + 10 pctAl_2O_3, (*b*) AlSi12 + 20 pctAl_2O_3, and (*c*) AlSi12 + 30 pctAl_2O_3.

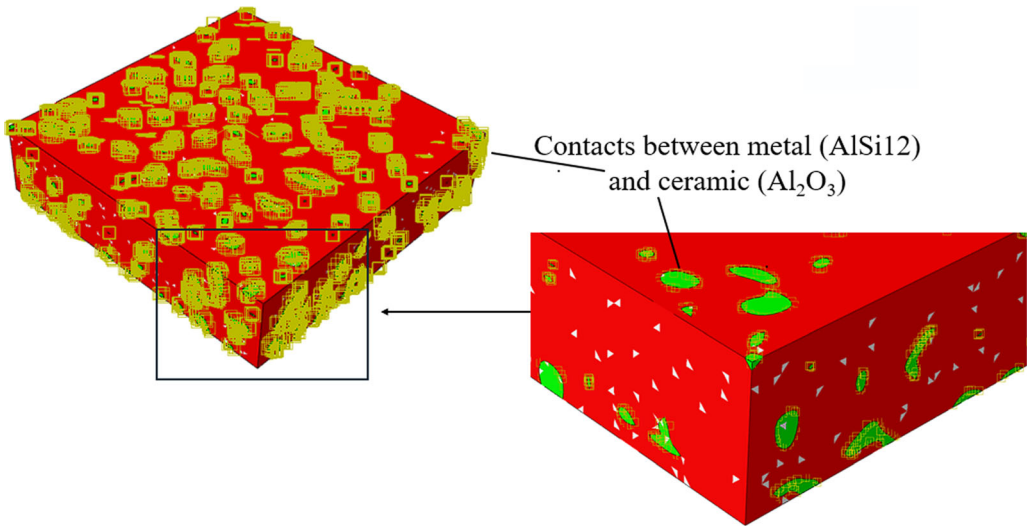

Fig. 7—FE model in Abaqus with interactions at the interface between AlSi12 and Al_2O_3 phases.

The effective thermal conductivity can be expressed as follows[52]:

$$\lambda_{\text{eff}} = \frac{Q}{A}\frac{L}{T_{\text{hot}} - T_{\text{cold}}}, \qquad [4]$$

where L is the length of the specimen, A is the cross-sectional area, $(T_{\text{hot}} - T_{\text{cold}})$ is the temperature difference across the bottom layer to the top layer of the specimen, Q is the overall heat flux obtained by integrating the fluxes across the inlet surface of the elements, expressed as follows:

$$Q = \int_A -\lambda \frac{\partial t}{\partial z} \mathrm{d}x\mathrm{d}y. \qquad [5]$$

The above equation was used for all the elements to calculate the thermal flux and the effective thermal conductivity. The thermal conductivity of the materials

used in the numerical computations were measured experimentally at room temperature and are listed in Table I.

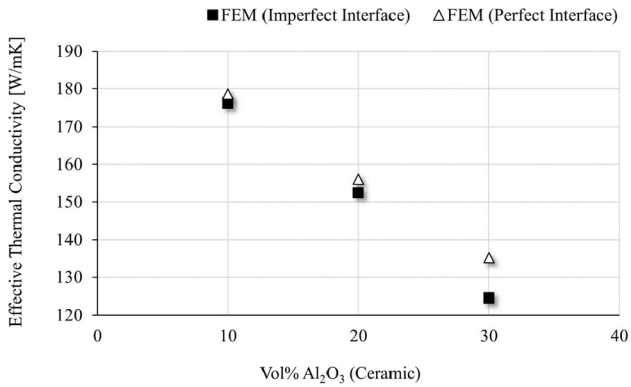

Fig. 8—Effect of imperfect interface on the effective thermal conductivity obtained from the micro-XCT-based FE model for different alumina volume fractions.

IV. RESULTS AND DISCUSSION

A. *Microstructure Characterization*

The scanning electron microscopy (SEM) images of the microstructure of the composite layers with 10, 20, and 30 vol pct Al_2O_3 prepared by the HP and SPS techniques are shown in Figure 11. The transition regions in the two-layer FGMs, sample D, sample E, and sample F (see Figure 2 for the notation used), are shown in Figures 12(a) through (c), respectively. The SEM observations reveal a uniform distribution of Al_2O_3 particles throughout the volume of the composite and good quality bonding at the interface between the two phases. The microstructures of the HP samples [Figures 11(a) through (c)] show smooth surfaces with almost no pores or cracks. The pores are barely visible in Figures 11(a) through (c) because the samples were almost completely consolidated during hot pressing. The HP sample with the lowest relative density (99.609 pct) is sample C with 30 pct Al_2O_3 content [Figure 11(c)]. Since the applied temperatures were much lower than those used for sintering Al_2O_3, we did not observe any

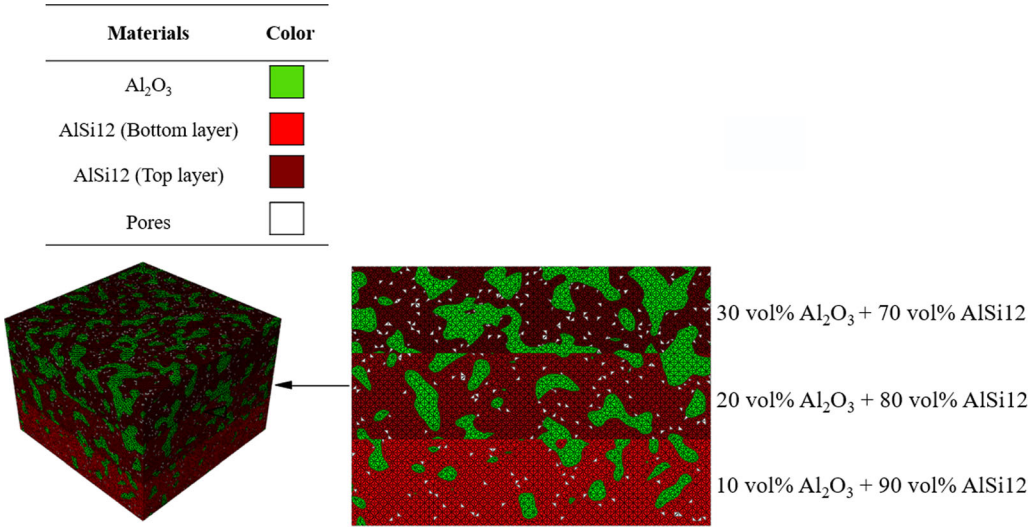

Fig. 9—Tetrahedron element mesh model generated with the ScanIP/FE software from the micro-XCT images for the three-layer FGM (sample G) fabricated by HP.

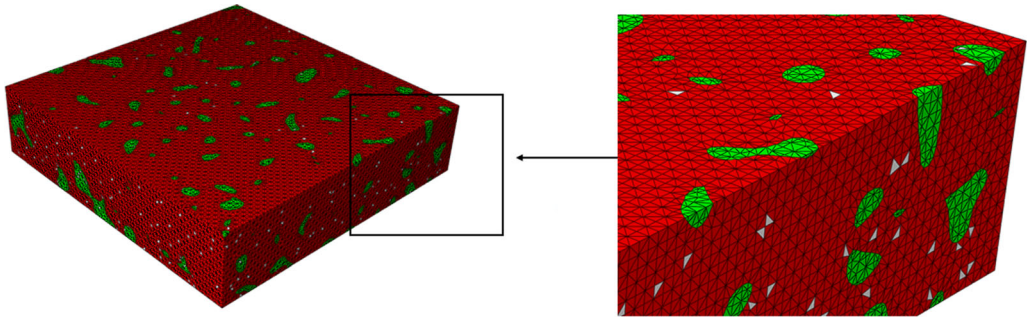

Fig. 10—Tetrahedron element mesh model generated with the ScanIP/FE software from the corresponding micro-XCT image for the single-layer composite (sample A) produced by the HP.

bonds between the ceramic grains. Therefore, for the purpose of numerical modeling, we considered the ceramic reinforcement as inclusions immersed in a metal matrix.

The cooling behavior of AlSi12 and Al_2O_3 was different as indicated by their thermal expansion coefficients. The in-house measured coefficient of thermal expansion was 23.7×10^{-6} (1/deg) for AlSi12 and 6.5×10^{-6} (1/deg) for Al_2O_3. As a result, the AlSi12 matrix was subject to tensile thermal stresses and was therefore more prone to pore formation than the alumina. Consequently, the pores were assumed to exist only in the metal matrix or at the interface between the reinforcement grains and the matrix. Due to the high plasticity of AlSi12, larger pores were flattened and the measured porosity of the material consisted mainly of nanometric pores, which are very difficult to detect. Micro-XCT is well suited to identify pores, but in the materials analyzed they were below the resolution of the Nanotom M device used in this study. The assumption that most of the pores exist in the AlSi12 matrix was confirmed to some extent by the volume distribution of nanopores obtained by the gas adsorption method. As will be shown later, the total volume of nanopores in the AlSi12 matrix was five times higher than in the alumina reinforcement.

The SEM micrographs of both HP and SPS samples [Figures 11(a) through (f)] show two distinct regions in the AlSi12 matrix. Since Si is characterized by limited solubility in Al, the SEM images show pure Al matrix with Si grains (black phases). Due to the different processing time, the size and number of Si grains in the HP and SPS samples are different. The irregularly shaped ceramic particles are visible as black grains with light contours [Figures 11(a) through (f)]. Note that the AlSi12 matrix is spatially continuous throughout the composite structure. This allows for heat dissipation as the AlSi12 matrix is the primary heat transfer material in these composites. For this reason, there is a significant decrease in the thermal conductivity of the composite samples as the ceramic content increases (see Table IV). Furthermore, the smooth transition between the composite layers observed in Figures 12(a) through (c), achieved during the sintering of the FGMs, explains the formation of a metallurgical bond that allows structural integrity between layers with different chemical compositions.

B. *Density of Composite Layers*

The carefully tuned parameters of the HP process made it possible to achieve relative density exceeding 99 pct for all samples of AlSi12/Al_2O_3 composites, as confirmed by density measurements shown in Table II. According to the DSC measurements performed, the melting point of the AlSi12 powder was approximately 590 °C, while the sintering temperature in the HP process was set at approximately 560 °C. This temperature, being not far from the melting point of AlSi12, caused the AlSi12 matrix to behave plastically, which in turn facilitated a defect-free pressing of hard alumina particles into a soft AlSi12 matrix under the pressure applied in the HP. A similar mechanism of consolidation in Al matrix composites has been reported in Reference 53. The combined effect of the sintering temperature of 560 °C and the pressure of 30 MPa resulted in almost complete consolidation of the AlSi12/Al_2O_3 composite layers sintered by the HP.

Generally, the SPS technique tends to produce materials that are well consolidated.[54] However, in the present study, the AlSi12/Al_2O_3 composites with 10, 20, and 30 vol pct of alumina consolidated by the SPS showed slightly lower relative densities to their HP counterparts (Table II). It should be recalled that the sintering temperature in the SPS process was set at 502 °C, which was significantly lower than in the HP case. This was the programmed temperature for SPS, but inside the mold the temperature may be a little higher. The reason for reducing the sintering temperature in the SPS process was the fact that when the programmed temperature was raised above 502 °C, the AlSi12 powder in the mold started to melt. This was due to the much higher heating rate in SPS (70 °C/min) compared to HP (5 °C/min), which caused a higher temperature gradient during heating. The temperature gradient of SPS resulted in a hot center and a colder outer volume due to Joule heating. In the case of HP, the temperature gradient was built up in the opposite direction. According to our observations from the laboratory, a higher temperature would lead to melting of the AlSi12, which was an undesirable scenario. On the other hand, the pressure applied in the SPS process was 40 MPa compared to 30 MPa in the HP process, but ultimately the relative densities of the SPS samples containing 10, 20, and 30 vol pct alumina were slightly lower than the corresponding composites prepared by the HP route, as shown in Table II.

The AlSi12/Al_2O_3 composites sintered by HP and SPS are almost fully dense (Table II), except for the SPS sample with the highest alumina content (30 pct). From the SEM images in Figure 13, it can be seen that the AlSi12 matrix in the AlSi12 + 30 pctAl_2O_3 (SPS) composite does not fill all the voids between the densely packed ceramic particles due to a shorter exposure to temperature. This is then reflected in the increased porosity of 2.49 pct of the AlSi12 + 30 pctAl_2O_3 (SPS) sample *vs* 0.39 pct AlSi12 + 30 pctAl_2O_3 (HP).

As mentioned in Section II–C, we also performed experiments based on the gas adsorption method to confirm or reject the assumption of the presence of nanopores in the HP-sintered AlSi12 and Al_2O_3 powders. The experiments on AutoSorbiQ, Quantachrome analyzer revealed the presence of nanopores in both AlSi12 and Al_2O_3 powders. The total pore volumes per unit mass in the diameter range (0.35 to 375 nm), which is close to the limits of the instrument, are shown in Table III. It is noted that the total volume of nanopores in the AlSi12 (HP) matrix is five times larger than that in the alumina phase.

C. *Thermal Conductivity of AlSi12*

Before discussing the thermal conductivity data obtained by the flash method for the AlSi12/Al_2O_3

Table I. Thermal Conductivities of the Phase Materials Used in the Numerical Models

Processing Route	Thermal Conductivity (W/mK)		
	AlSi12	Al_2O_3	Pores (Air)
Hot Pressing (HP)	204.8*	33.0*	0.025
Spark Plasma Sintering (SPS)	188.0*	33.0*	0.025

*Measured in-house on AlSi12 and Al_2O_3 sinters.

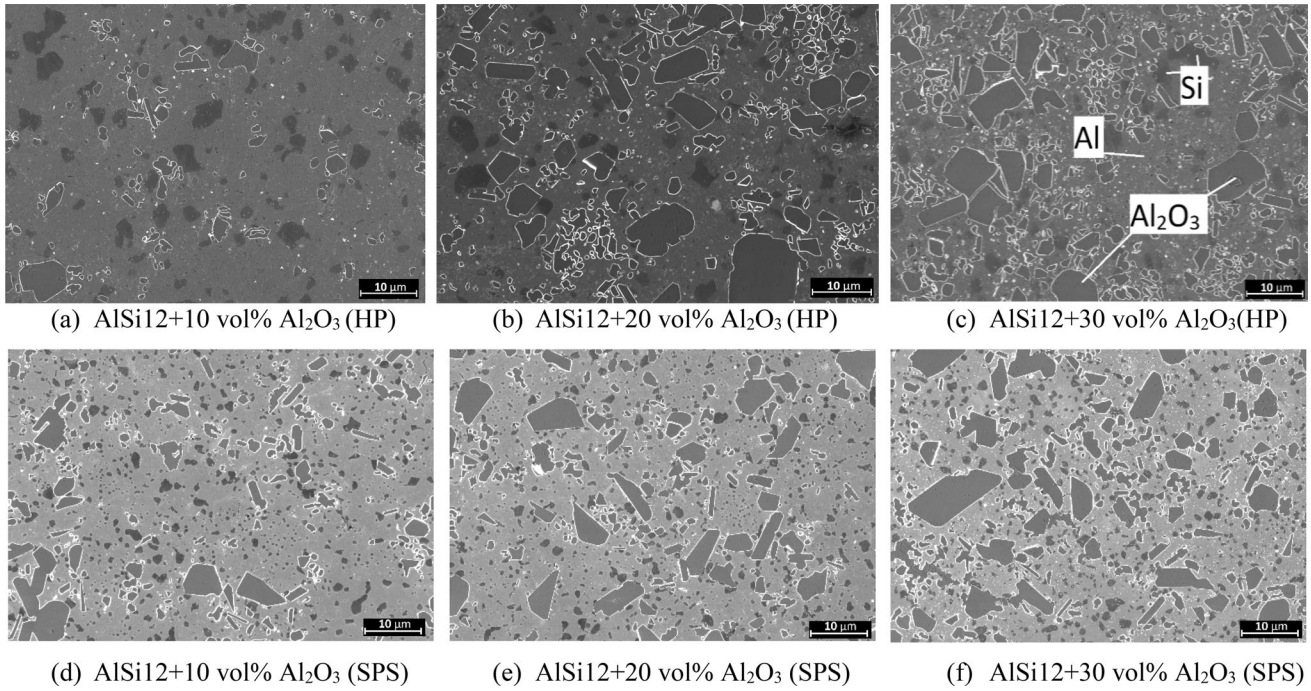

Fig. 11—SEM micrographs of HP-sintered AlSi12 with (*a*) 10 vol pct Al_2O_3, (*b*) 20 vol pct Al_2O_3, (*c*) 30 vol pct Al_2O_3 and SPS-sintered AlSi12 with (*d*) 10 vol pct Al_2O_3, (*e*) 20 vol pct Al_2O_3, and (*f*) 30 vol pct Al_2O_3.

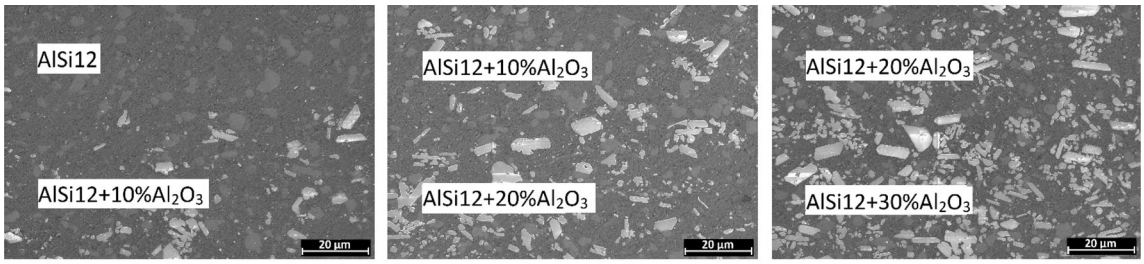

Fig. 12—SEM micrographs of the interlayer regions in HP-consolidated two-layer FGMs: (*a*) sample D, (*b*) sample E, and (*c*) sample F (according to the notation in Fig. 2).

composites and FGMs, it is first necessary to discuss a discrepancy noticed in the thermal conductivity measurements at room temperature (RT) for pure AlSi12 sintered by HP (204.8 W/mK) *vs* pure AlSi12 sintered by SPS (188.0 W/mK). As can be seen in Figure 14, this discrepancy is pronounced at RT and disappears as the temperature rises above 250 °C.

It was essential to find physical reasons for this behavior of the two AlSi12 sinters as it could affect all thermal conductivity data for AlSi12/Al_2O_3 composites and FGMs. The porosities of pure AlSi12 (HP) and AlSi12 (SPS) samples were negligible, as shown in Table II. Consequently, it could not be the reason for the difference in thermal conductivities of the two AlSi12 materials. The other hypothesis was that during the SPS and HP processes, which differed primarily by the heating rate (70 deg/min for SPS *vs* 5 deg/min for HP) and dwelling time (10 *vs* 180 minutes) but also in the sintering temperature (502 °C *vs* 560 °C due to the heating concept) and pressure (40 *vs* 30 MPa), some new

phases could have been formed that reduced the thermal conductivity of the SPS sample. However, this hypothesis was not supported by the EDX analysis performed on the AlSi12 (HP) and AlSi12 (SPS) samples.

On the other hand, the SEM analysis revealed that the average sizes of Al grains in the AlSi12 (HP) and AlSi12 (SPS) samples were distinctly different (Figure 15). Using the ASTM E112 grain size measurement procedure,[55] the average Al grain size was found to be 2.80 μm in the HP sample and 1.69 μm in the SPS sample. Also, the Si secondary phase in both samples shown in Figure 15 were of different sizes. It has been shown in the literature (*e.g.*, 56) that larger grains have higher intrinsic thermal conductivity. Grain size also controls the number of grain/grain boundaries and thus the interface thermal resistance, which is higher for fine-grained materials.[43,56] Consequently, the difference in thermal conductivity between the AlSi12 (HP) and AlSi12 (SPS) samples shown in Figure 12 could be attributed to these two effects related to the larger grain sizes in the HP samples than in the SPS samples. It should be noted that the grain growth effect, which is a drawback of the slow HP processes because it negatively affects the material strength, plays a positive role for heat transfer, which is evident from the higher thermal conductivity values for the AlSi12 (HP) samples shown in Figure 14.

The decrease in thermal conductivity of the AlSi12 (HP) sample with increasing temperature from RT to 300 °C (Figure 14) is typical behavior for metals, where thermal conductivity is mainly caused by the motion of free electrons. As the temperature increases, the molecular vibrations increase, which in turn decreases the mean free path of the molecules. As a result, they impede the movement of free electrons and reduce the thermal conductivity. On the other hand, the thermal conductivity behavior of the AlSi12 (SPS) sample in the temperature range of RT-300 °C initially shows an increasing tendency and a plateau around 150 °C. Several factors can affect the thermal conductivity of aluminum alloys, including the size of the aluminum grains as discussed above and the properties of the secondary phases.[57] To explain the effect of thermal conductivity variation of the AlSi12 (SPS) sample with temperature (Figure 14), we performed SEM analysis of the sample at RT and after heating it to 300 °C. The obtained SEM images [Figures 16(a), (b)] show no significant growth of Al grains[56] or spheroidization of Si precipitates[58] to account for an increase in thermal conductivity after heating to 300 °C.[56] However, some elliptical nanopores are visible at the boundaries of Al grains [Figure 16(a)], which disappeared after heat treatment [Figure 16(b)]. This pore annealing could lead to an increase in the thermal conductivity. The process of nanopores closure continued as the temperature increased which is reflected in the increasing conductivity AlSi12 (SPS) sample (Figure 14). At a certain temperature level (about 150 °C), the closure of the pores was complete and there was no further increase in the thermal conductivity (a plateau in Figure 14).

After heat treatment to 300 °C, the thermal conductivity of AlSi12 (HP) and AlSi12 (SPS) samples was again evaluated at RT. For the AlSi12 (HP) sample, it was equal to 200.3 [W/mK], which was lower than 208.4 [W/mK] obtained for this sample before heat treatment. On the other hand, for the AlSi12 (SPS) sample, it was equal to 196.4 [W/mK], which was higher than 188.3 [W/mK] obtained for this sample before heat treatment. Considering that the measurement error in this experiment was about 5 pct, it can be concluded that the RT thermal conductivity of AlSi12 (HP) and AlSi12 (SPS) samples after heat treatment approached the same level. This experimental fact can also be considered as an argument in favor of the nanopore annealing mechanism being responsible for thermal conductivity stabilization.

It should be noted that grain growth as such was not a subject of investigation in this work. However, the observed differences in grain structure in AlSi12 (HP) and AlSi12 (SPS) samples due to the different process conditions of HP and SPS provide a plausible explanation for the lower thermal conductivity of AlSi12 (SPS) compared to AlSi12 (HP) at room temperature.

In addition to the grain growth of AlSi12 caused by the sintering process, it may also occur when the AlSi12/Al_2O_3 composite is applied as a brake disk material. During intensive car braking, especially in high-performance cars, the temperature of the brake disk can significantly exceed 500 °C, and further grain growth of AlSi12 can occur, especially in the fine-grained AlSi12 (SPS) matrix material. This in turn will increase the thermal conductivity of AlSi12 (SPS) and bring it to the conductivity values of AlSi12 (HP). Detection of grain growth during car exploitation could be used as an indicator of thermal load on a brake disk. Knowing the initial AlSi12 grain size after sintering, any additional heat treatment will support grain growth. This idea may be more effective for the AlSi12 (SPS) as this material seems to have more potential for grain growth in the application phase.

Figure 17 shows an SEM micrograph of an area of pure AlSi12 sintered by HP together with the EDS map. The interfaces between the Si and Al grains are sharp and show no defects or pores. As the AlSi12 alloy powder was produced by the atomization process, a uniform distribution of elements was observed in the EDS analysis of the raw powder. During prolonged exposure to sintering temperature near the melting point of Al, precipitation of Si grains occurred according to the binary phase diagram of Al–Si. A smooth interface between the Si and Al grains in pure AlSi12 sintered by HP (Figure 17) improved the interfacial bond strength and increased the thermal conductivity of the sinter.[59] Therefore, it is understandable that the HP samples had a higher thermal conductivity in the temperature range RT-150 °C than the SPS samples directly after sintering. The higher thermal conductivity of the pure AlSi12 (HP) material carried over to the thermal conductivity of the composite layers and FGMs where this material was used as the matrix.

Table II. Measured Densities and Calculated Porosities of AlSi12/Al_2O_3 Composites Fabricated by HP and SPS

Material	Theoretical Density (g/cm^3)	Hot Pressing (HP)			Spark Plasma Sintering (SPS)		
		Measured Density (g/cm^3)	Relative Density (Pct)	Porosity (Pct)	Measured Density (g/cm^3)	Relative Density (Pct)	Porosity (Pct)
AlSi12	2.656	2.654	99.940	0.060	2.653	99.902	0.098
AlSi12 + 10vol pct Al_2O_3 (Sample A)	2.787	2.778	99.676	0.324	2.771	99.424	0.576
AlSi12 + 20vol pct Al_2O_3 (Sample B)	2.918	2.913	99.812	0.188	2.906	99.572	0.428
AlSi12 + 30vol pct Al_2O_3 (Sample C)	3.050	3.038	99.609	0.391	2.974	97.511	2.489

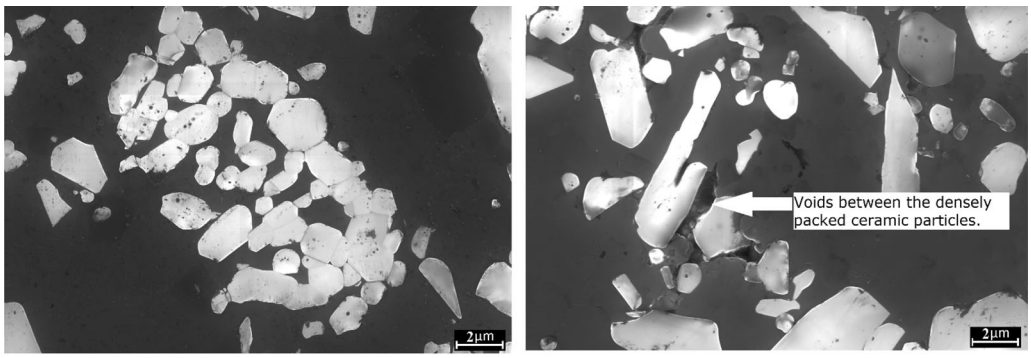

(a) (b)

Fig. 13—Porosity of AlSi12 + 30 pctAl_2O_3 samples sintered by (*a*) HP and (*b*) SPS.

Table III. Total Volume of Nanometric Pores and Average Pore Diameter in AlSi12 (HP) and Al_2O_3 Powders Measured by the Gas Adsorption Method

Sample	Total Pore Volume (cm^3/g)	Average Pore Diameter (nm)
AlSi12 (HP)	0.078	4.40
Al_2O_3	0.015	5.82

D. *Thermal Conductivity of Composite Layers and FGMs*

The thermal conductivity data obtained by the flash method for the AlSi12/Al_2O_3 layered composites with different alumina volume fractions in the temperature range RT-300 °C are summarized in Table IV. The most interesting case of the three-layer FGMs (sample G) prepared by HP or SPS is graphically shown in Figure 18.

From the analysis of the data for the single-layer composites in Table IV, it is evident that increasing the volume fraction of alumina, sample A (10 pct), sample B (20 pct), and sample C (30 pct), decreases the thermal conductivity of the composite layer. This effect is observed for both the HP and SPS samples over the entire temperature range of the experiment, although it is more pronounced at lower temperatures. Another observation from Table IV is that the thermal conductivities directly after sintering of the single-layer samples (A, B, C) sintered by HP are consistently higher than their SPS counterparts (D, E, F). This may be related to a combination of two effects: (i) the effect discussed above that the AlSi12 (SPS) matrix material has a lower thermal conductivity than AlSi12 (HP) (see Figure 14), and (ii) the effect of the higher porosity of the SPS samples (D, E, F) compared to the HP samples (A, B, C) as seen in Table II. Similar behavior to the single-layer composites is observed in Table IV in the two-layer HP and SPS composite samples D, E, F, with ceramic volume contents of 0/10, 10/20, and 20/30 pct, respectively. It should be noted that the two-layer samples D and E, both HP and SPS, had the highest thermal conductivities of all the samples tested. The thermal conductivity of the three-layer FGM (sample G) was consistently higher than that of the two-layer FGM (sample F) throughout the temperature range of the experiment.

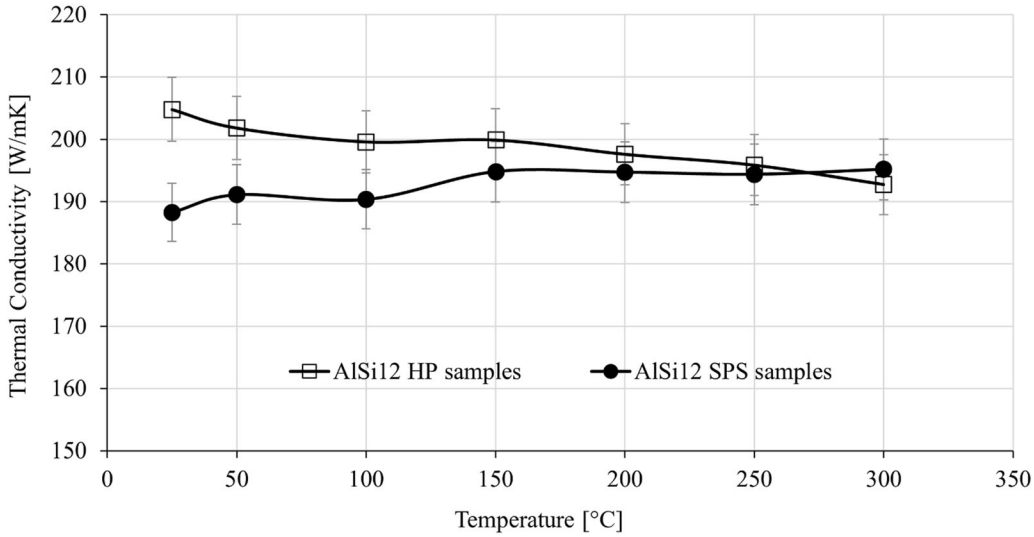

Fig. 14—Measured thermal conductivity of unreinforced AlSi12 samples sintered with HP and SPS in the temperature range RT-300 °C.

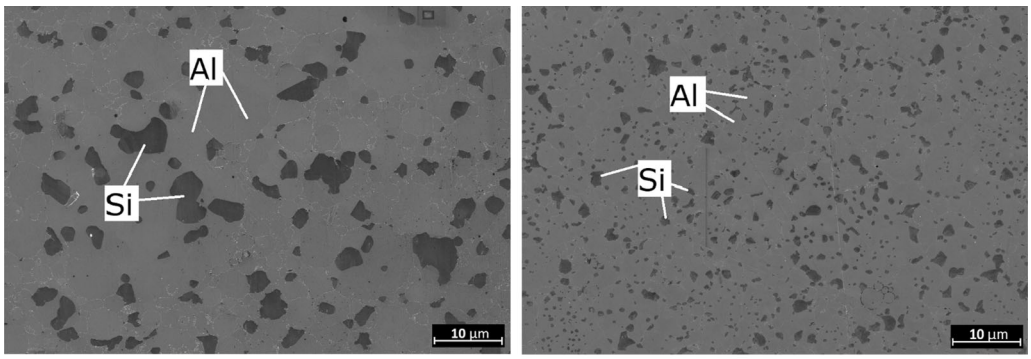

(a) (b)

Fig. 15—SEM micrographs of unreinforced AlSi12 samples sintered by (*a*) HP and (*b*) SPS.

Figure 18 shows the variability of the thermal conductivity (λ) data of the three-layer HP and SPS FGM samples over the temperature range RT-300 °C. As mentioned above, the FGM produced by HP has a significantly higher thermal conductivity than that produced by SPS over the entire temperature range, with a difference of 22 pct at RT. Also, a systematic but slight decrease in λ is observed with increasing temperature. This effect is more pronounced for the HP samples.

Figure 19 shows the comparison of the experimentally measured thermal conductivity for the two-layer FGM samples (D, E, F) and the three-layer FGM sample G obtained by HP, with that of gray cast iron over the temperature range RT-300 °C. Gray cast iron is a conventional material used in the manufacture of brake disks for passenger cars. From Figure 19 it can been seen that the thermal conductivity of the three-layer FGM (sample G) exceeds the thermal conductivity of gray cast iron by a factor of 3 in the temperature range RT-300 °C, which is favorable for the rapid dissipation of heat from the braking system. Under normal braking conditions, the temperature of the brake disks varies between 150 °C and 250 °C. However, in high-performance cars or under extreme thermomechanical loading, the operating temperature in the brake disk/pad pair can temporarily reach 500 °C or higher. The aluminum matrix composites reinforced with SiC or alumina particles have recently become commercially available for brake disks. They can be used in vehicles where the maximum operating temperature does not exceed 450 °C making them suitable to small cars or rear brakes.[60] Other solutions for Al-based brake disks include integration of ceramic matrix composites (CMCs) and an Al alloy.[61]

It should also be noted from Figure 19 that graded composites produced by hot pressing maintain almost constant thermal conductivity over the entire temperature range RT to 300 °C. This is in contrast to the results reported in Reference 9 for an AlSi12/Al_2O_3 interpenetrating phase composite (IPC) produced by pressure-assisted infiltration of a molten AlSi12 alloy

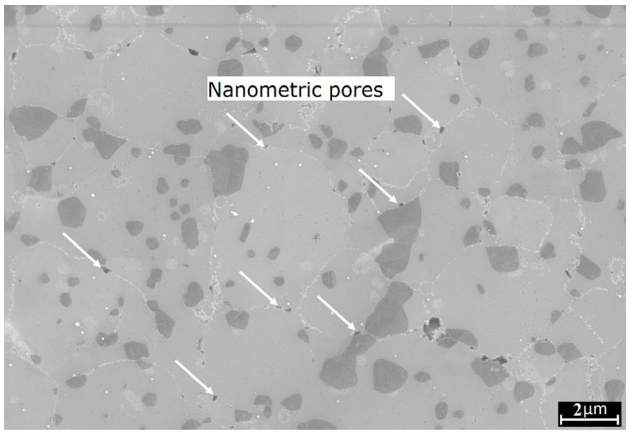

(a)

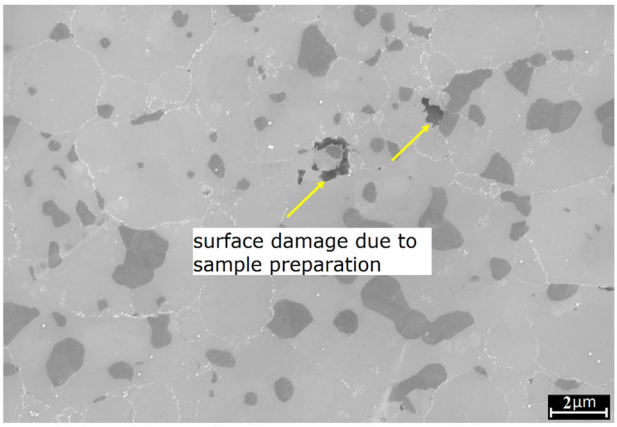

(b)

Fig. 16—SEM images of (*a*) AlSi12 (SPS) sample at RT with nanopores visible at Al grain boundaries as indicated by arrows, (*b*) AlSi12 (SPS) sample after heat treatment at 300 °C without nanopores; white arrows in image (b) indicate surface damage caused by sample preparation for SEM.

into a porous ceramic preform, where the thermal conductivity decreased with increasing temperature from RT to 300 °C.

E. *Thermal Conductivity of Composites and FGMs: Comparison with Modeling Results*

The thermal conductivity data obtained by the flash method were used to validate the micro-XCT FEM model introduced in Section III. Figure 20 shows a comparison of the results obtained from the micro-XCT FEM model with the experimental data for three single-layer composites (samples A, B, C) consolidated by hot pressing. It is noted that the micro-XCT FEM model predicts the experimental data for all the samples with remarkable accuracy (relative error less than 4 pct).

Figure 21 shows a comparison of the numerical simulations by the micro-XCT FEM model with the experimental results of the thermal conductivity at RT for the two-layer FGMs with 0/10, 10/20, 20/30 pct alumina (samples D, E, F) and the three-layer FGM with 10/20/30 pct alumina (sample G) fabricated by the HP. Similar to the single-layer case, the agreement between the numerical simulations and the experimental results for the two- and three-layer FGMs is good, with a relative error of less than 6 pct. The error bars shown in Figures 20 and 21 correspond to a 5 pct error based on the precision of the instruments used to measure thermal diffusivity by the flash method.

In addition to the numerical simulations by the micro-XCT FEM model, in Figure 21 we have added the Reuss estimates of the thermal conductivities for the two- and three-layer FGMs calculated using Eq. [2]. It can be seen that the Reuss estimates are surprisingly close to the experimental data. Therefore, the Reuss model for composite layers connected in series can be used as a fast approximation of the thermal conductivity of the layered MMCs.

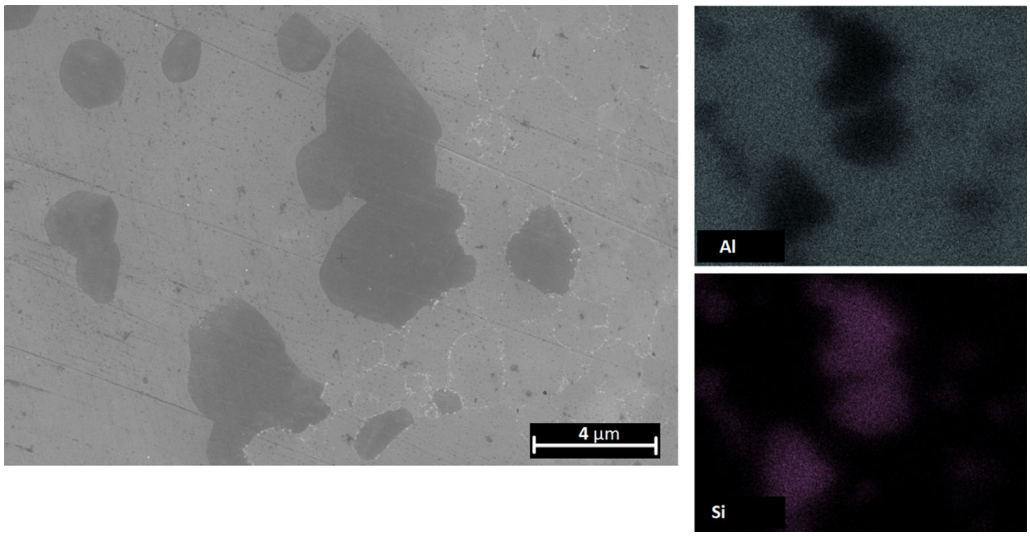

Fig. 17—SEM micrograph showing interfaces between Si and Al grains in HP-sintered AlSi12 sample (left) and EDS map (right).

Table IV. Measurements of the Thermal Conductivity (λ) of AlSi12 Matrix Layered Composites Reinforced with Different Volume Fractions of Al_2O_3 in the Temperature Range 25 °C (RT) to 300 °C

	Thermal Conductivity of HP Samples, λ (W/mK)						
	Single Layer			Two-Layer			Three-Layer (FGM)
T (°C)	Sample A	Sample B	Sample C	Sample D	Sample E	Sample F	Sample G
25	169.99	138.75	123.69	180.86	162.31	136.73	147.09
50	167.25	138.32	122.55	181.11	160.07	136.13	146.72
100	166.34	134.80	119.76	178.01	159.27	133.58	143.54
150	165.02	134.30	118.91	176.93	157.62	132.42	142.73
200	163.44	131.62	116.45	175.25	155.02	129.62	140.45
250	164.22	129.36	113.66	175.09	155.69	127.14	138.11
300	163.98	129.43	112.78	175.54	154.32	126.84	137.51
	Thermal Conductivity of SPS Samples, λ (W/mK)						
	Single Layer			Two-Layer			Three-Layer (FGM)
	Sample A	Sample B	Sample C	Sample D	Sample E	Sample F	Sample G
25	141.33	118.14	95.41	165.04	133.05	110.58	119.89
50	142.21	119.94	97.13	166.04	133.30	110.55	118.90
100	144.53	120.54	97.90	165.02	134.42	110.17	119.34
150	144.99	120.94	97.42	168.53	138.07	110.66	117.86
200	146.29	120.34	96.84	169.12	138.11	109.97	116.44
250	147.51	120.04	96.46	170.02	139.29	109.62	117.34
300	148.89	120.58	94.88	171.31	140.72	108.78	116.42

Sample labels (A through G) refer to those in Fig. 2.

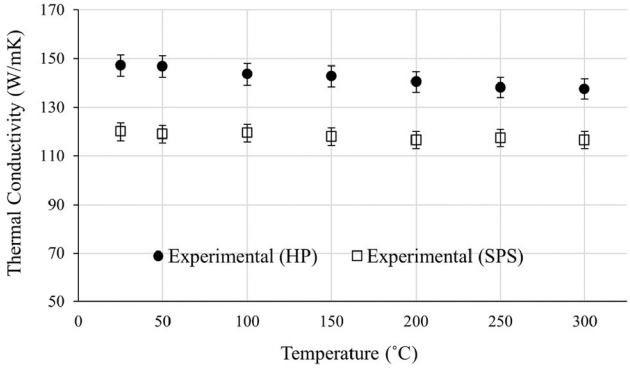

Fig. 18—Results of thermal conductivity measurements of three-layer FGMs (sample G in Fig. 2) fabricated by HP and SPS in the temperature range from RT to 300 °C.

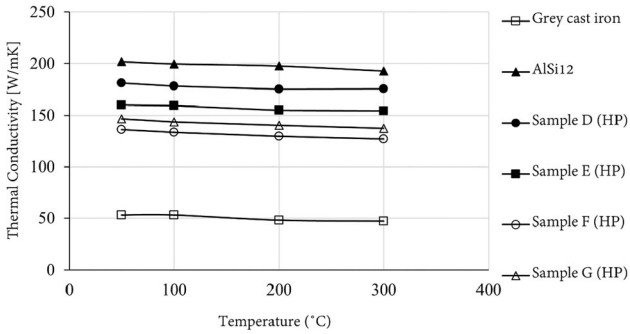

Fig. 19—Comparison of the experimentally measured thermal conductivities of the two-layer FGMs (samples D, E, F), the three-layer FGM (sample G) fabricated by HP, and the gray cast iron used in brake disks.

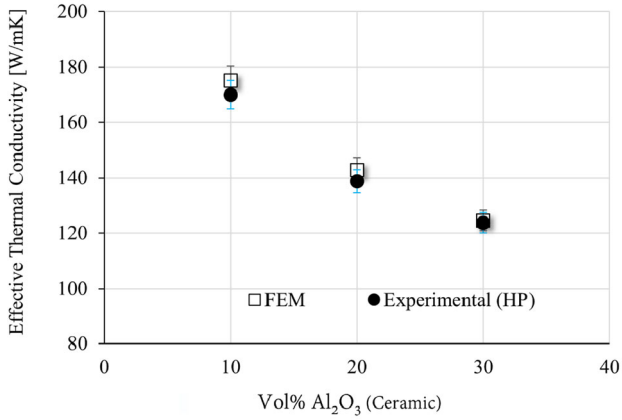

Fig. 20—Comparison of the micro-XCT FEM model with experimental results of the thermal conductivity of single-layer AlSi12/Al_2O_3 (HP) composites with 10, 20, and 30 vol pct of alumina (samples A, B, C) at room temperature.

V. CONCLUSIONS

This work is a combined experimental and modeling study to evaluate the thermal conductivity of AlSi12/Al_2O_3-layered composites prepared by hot pressing (HP) and spark plasma sintering (SPS). The relative densities of the fabricated materials were above 99 pct for the HP and above 97 pct for the SPS samples. An increase in porosity was observed as the volume fraction of ceramic reinforcement increased from 10 to 30 pct. Porosity in the composite structure and an increase in interfacial thermal resistance resulted in a decrease in

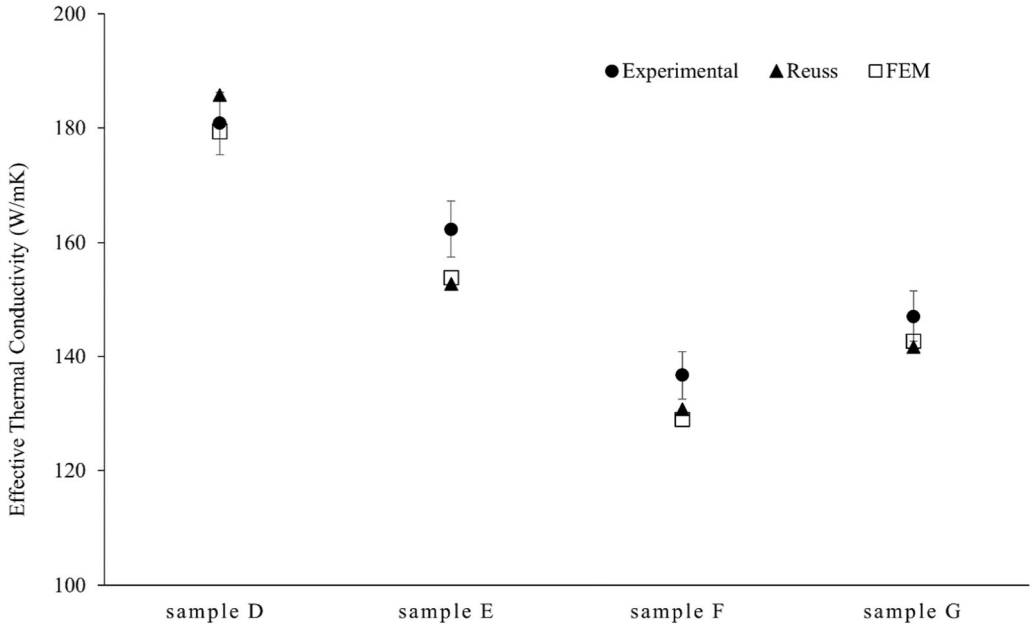

Fig. 21—Comparison of micro-XCT FEM results and Reuss estimates [Eq. 2] with experimental measurements at room temperature of thermal conductivity for two-layer FGMs (samples D, E, F) and the three-layer FGM (sample G) fabricated by the HP.

thermal conductivity. A discrepancy was observed in the thermal conductivity of pure AlSi12 (HP) and AlSi12 (SPS) samples measured immediately after sintering. A difference in grain size revealed by SEM analysis was the main reason why the thermal conductivity of SPS samples was lower than that of HP samples.

Accurate predictions of the thermal conductivity, with a relative error of less than 4 pct for single-layer and 6 pct for two- and three-layer composites, were obtained from the proposed micro-XCT-based FEM model, where micro-XCT images of the actual material microstructure were used to develop finite element meshes. Unlike the micromechanical models, the micro-XCT-based FEM model makes no assumptions about geometrical characteristics of the material microstructure and can be used to predict the thermal conductivity of other composites or different composition gradients provided that the micro-XCT technique is suitable for these materials. It should be added that the simple Reuss estimate of the effective thermal conductivity of the layered materials was very close to the results obtained from the more complex micro-XCT-based FEM model. Therefore, it is recommended for use when a fast estimate of the effective thermal conductivity of the layered metal–ceramic composites is required.

ACKNOWLEDGMENTS

The financial support from the National Science Centre, Poland, within research Project No. 2019/35/B/ST8/03131) is acknowledged. The authors would like to thank Jördis Rosc and Roland Brunner from Materials Center Leoben (Austria) for performing the micro-XCT experiments.

CONFLICT OF INTEREST

The authors declare that they have no conflict of interest.

OPEN ACCESS

REFERENCES

1. M. Sathish, N. Radhika, and B. Saleh: *Composites B*, 2021, vol. 225, p. 109278.
2. K. Kokini and Y. Takeuchi: *Mater. Sci. Eng. A*, 1993, vol. 189, pp. 301–09.
3. B. Saleh, J. Jiang, R. Fathi, T. Al-Habibi, Q. Xu, L. Wang, D. Song, and A. Ma: *Composites B*, 2020, vol. 201, p. 108376.
4. P. Kumar, S.K. Sharma, and R.K. Raj Singh: *Mater. Manuf. Process.*, 2023, vol. 38, pp. 1033–67.
5. A. Strojny-Nędza, K. Pietrzak, and W. Węglewski: *J. Mater. Eng. Perform.*, 2016, vol. 25, pp. 3173–84.

6. F.F. Kamaruzaman, D.M. Nuruzzaman, M.A. Chowdhury, S.N.S. Jamaludin, S. Basri, and N.M. Ismail: *Int. J. Mater. Prod. Technol.*, 2019, vol. 59, pp. 48–62.
7. C. Tatar and N. Özdemir: *Phys. B*, 2010, vol. 405, pp. 896–99.
8. J. Maj, W. Węglewski, K. Bochenek, Ł Rogal, S. Woźniacka, and M. Basista: *Metall. Mater. Trans. A*, 2021, vol. 52A, pp. 4727–36.
9. J. Maj, M. Basista, W. Węglewski, K. Bochenek, A. Strojny-Nędza, K. Naplocha, T. Panzner, M. Tatarková, and F. Fiori: *Mater. Sci. Eng. A*, 2018, vol. 715, pp. 154–62.
10. D.M. Nuruzzaman, A.K.M.A. Iqbal, M. Marzuki, M.A. Chowdhury, N.M. Ismail, M.I.A. Latiff, Md.M. Rahman, and M.A. Gebremaram: *iMEC-APCOMS 2019: Proc. 4th Int. Manuf. Eng. Conf. 5th Asia Pac. Conf. Manuf. Syst*. 2020. pp. 478–83.
11. S. Farahmand, A.H. Monazzah, and M.H. Soorgee: *Ceram. Int.*, 2019, vol. 45, pp. 22775–82.
12. M.J. Oza, K.G. Schell, E.C. Bucharsky, T. Laha, and S. Roy: *Mater. Sci. Eng. A*, 2021, vol. 805, p. 140625.
13. Y. Guo, W. Li, X. Liu, K. Sugio, W. Liu, A.S. Suzuki, and G. Sasaki: *Mater. Sci. Eng. A*, 2023, vol. 872, p. 145010.
14. S. Farahmand, M.H. Soorgee, and A.H. Monazzah: *Ceram. Int.*, 2021, vol. 47, pp. 24906–15.
15. N. Sindhu, R.K. Goyal, and V.M. Sreekumar: *Metall. Mater. Trans. A*, 2024, vol. 55A, pp. 1654–72.
16. E. Jayakumar, J.C. Jacob, T.P.D. Rajan, M.A. Joseph, and B.C. Pai: *Metall. Mater. Trans. A*, 2016, vol. 47A, pp. 4306–15.
17. G. Sahragard-Monfared, C.M. Smudde, R.D. Carpenter, Z.A. Munir, and J.C. Gibelin: *Metall. Mater. Trans. A*, 2023, vol. 54A, pp. 3594–602.
18. K. Dash, D. Chaira, and B.C. Ray: *Mater. Res. Bull.*, 2013, vol. 48, pp. 2535–42.
19. D. Garbiec, M. Jurczyk, N. Levintant-Zayonts, and T. Mościcki: *Arch. Civ. Mech. Eng.*, 2015, vol. 15, pp. 933–39.
20. P. Gudlur, A. Forness, J. Lentz, M. Radovic, and A. Muliana: *Mater. Sci. Eng. A*, 2012, vol. 531, pp. 18–27.
21. R. Madan and S. Bhowmick: *World J. Eng.*, 2022, vol. 19, pp. 291–301.
22. Y.M. Shabana and N. Noda: *Int. J. Solids Struct.*, 2008, vol. 45, pp. 3494–506.
23. A. Strojny-Nędza, K. Pietrzak, M. Teodorczyk, M. Basista, W. Węglewski, and M. Chmielewski: *Arch. Metall. Mater.*, 2017, vol. 62, pp. 1311–14.
24. P. Gudlur, A. Muliana, and M. Radovic: *Composites B*, 2014, vol. 58, pp. 534–43.
25. J.M. Molina and E. Louis: *J. Alloys Compd.*, 2018, vol. 736, pp. 246–54.
26. P.E. Hopkins: *ISRN Mech. Eng.*, 2013, vol. 2013, p. 682586.
27. A. Giri and P.E. Hopkins: *Adv. Funct. Mater.*, 2020, vol. 30, p. 1903857.
28. N. Ferguen, C. Cogné, E. Bellenger, M. Guessasma, and C. Pélegris: *J. Compos. Mater.*, 2013, vol. 47, pp. 3311–21.
29. M. Chmielewski and W. Węglewski: *Bull. Pol. Acad. Sci.: Tech. Sci.*, 2013, vol. 61, pp. 507–14.
30. M.S. Charan, A.K. Naik, N. Kota, T. Laha, and S. Roy: *Int. Mater. Rev.*, 2022, vol. 67, pp. 797–863.
31. M. Nižňanský, K. Vanmeensel, J. Vleugels, V. Tyrpekl, and M. Vilémová: *Open Ceram.*, 2023, vol. 16, p. 100433.
32. M. Basista, W. Węglewski, K. Bochenek, Z. Poniżnik, and Z. Nowak: *Adv. Eng. Mater.*, 2017, vol. 19, p. 1700098.
33. A. Majeed, M. Muzamil, J. Lv, B. Liu, and F. Ahmad: *J. Braz. Soc. Mech. Sci. Eng.*, 2019, vol. 41, p. 267.
34. S. Khoshsima, A.Z. Alshemary, A. Tezcaner, S. Surdem, and Z. Evis: *Process. Appl. Ceram.*, 2018, vol. 12, pp. 143–52.
35. A. Reuss: *J. Appl. Math. Mech.*, 1929, vol. 9, pp. 49–58.
36. ABAQUS Analysis User's Manual, Version 6.6. Hibbett, Karlsson and Sorensen Inc., Pawtucket, RI, 2006.
37. Simpleware Software ScanIP/FE v.4.3, Simpleware Ltd., Exeter, 2011.
38. W. Węglewski, P. Pitchai, K. Bochenek, G. Bolzon, R. Konetschnik, B. Sartory, R. Ebner, D. Kiener, and M. Basista: *Metall. Mater. Trans. A*, 2020, vol. 51A, pp. 2377–90.
39. G.S. Campbell and J.M. Norman: *An Introduction to Environmental Biophysics*, 2nd ed. Springer-Verlag, New York, 1998, p. 118.
40. T. Andritsch. PhD Thesis, Delft University of Technology, Delft, Netherlands, 2010, pp. 51–53.
41. D. Marcos-Gómez, J. Ching-Lloyd, M.R. Elizalde, W.J. Clegg, and J.M. Molina-Aldareguia: *Compos. Sci. Technol.*, 2010, vol. 70, pp. 2276–83.
42. D. Yan-Jun, G. Jian-Jun, R. Xing-Jie, F. Bai, F. Wen-Zhen, and T. Wen-Quan: *Appl. Energy*, 2018, vol. 228, pp. 1601–17.
43. M. Kida, L. Weber, C. Monachon, and A. Mortensen: *J. Appl. Phys.*, 2011, vol. 109, p. 064907.
44. J.C. Maxwell: *A Treatise on Electricity and Magnetism*, vol. 1, 3rd ed., Dover, New York, 1954, pp. 9–30.
45. D.A.G. Bruggeman: *Ann. Phys.*, 1935, vol. 24, p. 665.
46. M.G. Muraleedharan, K. Gordiz, S. Ju, J. Shiomi, V. Yang, and A. Henry: arXiv:1807.06631, 2018, pp. 1–25.
47. R. Stoner and H. Maris: *Phys. Rev. B*, 1993, vol. 48, p. 16373.
48. P.E. Hopkins, R. Salaway, R. Stevens, and P. Norris: *Int. J. Thermophys.*, 2007, vol. 28, pp. 947–57.
49. P.E. Hopkins, T. Beechem, J.C. Duda, K. Hattar, J.F. Ihlefeld, M.A. Rodriguez, and E.S. Piekos: *Phys. Rev. B*, 2011, vol. 84, p. 125408.
50. R. Cao, J.X. Jiang, C. Wu, and X.S. Jiang: *IOP Conf. Ser.: Mater. Sci. Eng.*, 2017, vol. 213, pp. 12001–09.
51. H. Asraful, S. Shekhar, S.V.S.N. Murty, J. Ramkumar, K. Kar, and K. Mondal: *Adv. Powder Technol.*, 2018, vol. 29, pp. 3427–39.
52. J. Floury, J. Carson, and Q. Tuan Pham: *Food Bioprocess Technol.*, 2008, vol. 1, pp. 161–70.
53. A. Kurzawa, D. Pyka, K. Jamroziak, M. Bocian, P. Kotowski, and P. Widomski: *Compos. Struct.*, 2018, vol. 201, pp. 834–44.
54. M. Abedi, S. Sovizi, A. Azarniya, D. Giuntini, M.E. Seraji, H.R.M. Hosseini, Ch. Amutha, S. Ramakrishna, and A. Mukasyan: *Crit. Rev. Solid State Mater. Sci.*, 2023, vol. 48, pp. 169–214.
55. ASTM E112-96, *Standard Test Methods for Determining Average Grain Size*, Reapproved 2004 e2, 2004, pp. 10–11.
56. D.S. Smith, F. Puech, B. Nait-Ali, A. Alzina, and S. Honda: *Int. J. Heat Mass Transf.*, 2018, vol. 121, pp. 1273–80.
57. A. Zhang and Y. Li: *Materials*, 2023, vol. 16, p. 2972.
58. J.K. Chen, H.Y. Hung, C.F. Wang, and N.K. Tang: *Int. J. Heat Mass Transf.*, 2017, vol. 105, pp. 189–95.
59. X. Zi-yang, C. Guo-qin, W. Gao-hui, Y. Wen-shu, and L. Yan--mei: *Trans. Nonferrous Met. Soc. China*, 2010, vol. 21, pp. 2134–38.
60. A.J. Day and D. Bryant: *Braking of Road Vehicles*, 2nd ed. Elsevier Science, Amsterdam, 2022, p. 439.
61. V. Casalegno, F. Smeacetto, M. Salvo, M. Sangermano, F. Baino, C. Noé, M. Orlandi, R. Piavani, R. Bonfanti, and M. Ferraris: *Ceram. Int.*, 2021, vol. 47, pp. 3463–73.